ADVANCED ENERGY MATERIALS
www.advenergymat.de

Mitigating Intrinsic Interfacial Degradation in Semi-Transparent Perovskite Solar Cells for High Efficiency and Long-Term Stability

Syed Dildar Haider Naqvi, Kyungnan Son, Wonzee Jung, Hui ung Hwang, Sangmin Lee, Arheum Lee, Minjong Keum, Sunwook Kim, Jeong Won Kim, Min Gu Kang, Hee-eun Song, Sungjun Hong, Inyoung Jeong, Seungkyu Ahn, Andreas Lambertz, Kaining Ding, Weiyuan Duan, Kanghoon Yim,* and SeJin Ahn**

Conventional semi-transparent perovskite solar cells (ST-PSCs) generally exhibit inferior performance and stability relative to opaque PSCs. However, a comprehensive understanding of the origins of inferior performance and stability of ST-PSCs and a practical solution to these challenges are both lacking. Here, it is shown for the first time that lithium ions from a lithium bis(trifluoromethanesulfonyl)imide (LiTFSI)-doped 2,2′,7,7′-tetrakis[N,N-di(4-methoxyphenyl)amino]−9,9′-spirobifluorene (Spiro-MeOTAD) hole-transport layer (HTL) can diffuse into the molybdenum trioxide buffer layer at their interface, yielding ST-PSCs with lower efficiency and accelerated degradation. It is also demonstrated that this undesired Li-ion diffusion can be avoided by HTL surface modification with stable lithium oxides. Using this approach, the constructed ST-PSC exhibits a new record power conversion efficiency (PCE) of 22.02% (21.68% certified) and a fill factor of >80%, with >99% shelf-stability after 400 h and >99% operational stability for 240 h, which clears away this longstanding limitation of the performance and stability of ST-PSCs. This strategy is also applied to fabricate four- and two-terminal perovskite/silicon tandem solar cells with bifacial equivalent efficiencies of 31.5% and 26.34%, respectively, at 20% albedo.

1. Introduction

The power conversion efficiency (PCE) of conventional (n-i-p) opaque perovskite solar cells (PSCs) has increased remarkably from 3.81% in 2009,[1] to a certified 25.8% in 2023.[2] This enhancement was achieved by taking advantage of the excellent optoelectronic properties of perovskite absorbers, e.g., their high absorption coefficients, sharp optical absorption edges, tunable bandgaps, and long-diffusion lengths. As a result, perovskite photovoltaics have become an attractive option for widespread applications across various fields, including building-integrated photovoltaics (BIPV) as power-generating windows in buildings,[3] or as the top cell in tandem solar cells.[4] However, these applications require the PSCs to have a certain degree of transparency in specific wavelength regions; thus, the conventional opaque metal back

S. D. H. Naqvi, K. Son, S. Lee, A. Lee, M. G. Kang, H.-eun Song, S. Hong, I. Jeong, S. Ahn, S. Ahn
Department of Photovoltaics Research
Korea Institute of Energy Research
Daejeon 34125, Republic of Korea
E-mail: swisstel@kier.re.kr

S. D. H. Naqvi, S. Hong, S. Ahn
Department of Renewable Energy and Engineering
University of Science and Technology
Daejeon 34113, Republic of Korea

The ORCID identification number(s) for the author(s) of this article can be found under https://doi.org/10.1002/aenm.202302147

DOI: 10.1002/aenm.202302147

W. Jung, K. Yim
Energy AI & Computational Science Laboratory
Korea Institute of Energy Research
Daejeon 34129, Republic of Korea
E-mail: khyim@kier.re.kr

W. Jung
Department of Physics
Chungnam National University
Daejeon 34134, Republic of Korea

H. ung Hwang, J. W. Kim
Operando Methodology and Measurement Team
Korea Research Institute of Standards and Science
Daejeon 34113, Republic of Korea

H. ung Hwang, J. W. Kim
Department of Nano Science
University of Science and Technology
Daejeon 34113, Republic of Korea

electrode must be replaced by a transparent one. In general, the PSCs fabricated by employing transparent back electrodes instead of opaque metal electrodes are termed as semi-transparent (ST)-PSCs[4–9] regardless of their transparency at specific wavelengths, i.e., in visible or near-infrared (NIR) region of the solar spectrum. Thus, ST-PSCs throughout this manuscript refer to the PSCs with transparent back electrodes.

To construct ST-PSCs, researchers have proposed various transparent electrode structures, including carbon-based films,[10,11] transparent metal electrodes,[7,9,12,13] and transparent conducting oxide (TCO)-based structures.[4,14] The ST-PSCs with the highest PCE (21.4%) were prepared via the mechanical joining of a semi-cell stack and an indium tin oxide (ITO) electrode,[15] mediated by a carbon nanotube slurry. However, from a commercialization perspective, ST-PSCs with TCO electrodes deposited directly onto the cell stack are considered the most promising and practical, primarily because TCOs can be deposited using an industrially mature sputtering process. Chen et al. fabricated an ST-PSC with a PCE of 19.4% using a sputter-deposited indium-doped zinc oxide (IZO) electrode.[4] However, special consideration must be given to prevent the sputter damage of the hole-transport layer (HTL) because the PSCs yielding record-breaking PCEs in recent years reportedly used an organic small molecule, namely 2,2′,7,7′-tetrakis[*N*,*N*-di(4-methoxyphenyl)amino]−9,9′-spirobifluorene (Spiro-MeOTAD), as HTL.[16–18] Therefore, to prevent sputter-damage to the organic HTL, an inorganic buffer layer, usually molybdenum trioxide (MoO_3), is deposited onto the HTL via thermal evaporation before the TCO sputter-deposition.[19,20] As a result, the HTL/back electrode structure changes from Spiro-MeOTAD/Gold(Au) in opaque PSCs to Spiro-MeOTAD/MoO_3/TCO in TCO-based ST-PSCs. However, a literature survey (Table S1, Supporting Information) indicated that replacing Au in opaque PSCs with MoO_3/TCO in ST-PSCs often reduces the PCE owing to the lower short-circuit current density (J_{sc}) and fill factor (FF) in ST-PSCs relative to the opaque PSCs. The J_{sc} loss in ST-PSCs is due to the lack of back-reflection from the opaque Au electrode, which can be minimized by increasing the thickness of the absorber layer.[4] However, lower FF values in ST-PSCs need a comprehensive understanding of fundamental charge transport characteristics of MoO_3/TCO structure, yet this aspect has not been thoroughly investigated. Notably, a FF of 80% or higher is routinely reported for state-of-the-art opaque PSCs (Table S2, Supporting Information), whereas the best reported FF value to our knowledge for ST-PSCs with MoO_3/TCO structures is 77.7%.[4] The origin of the relatively lower FF observed in MoO_3/TCO-based ST-PSCs is not fully understood. Based on the literature survey in Tables S1 and S2, Supporting Information, we benchmark the high FF to be 80% or higher and low FF to be less than 80% for the sake of discussion in this study.

In addition to the lower efficiency of ST-PSC, device stability is an issue of tremendous importance. There have been several reports investigating degradation of opaque PSCs under various stresses such as moisture,[21,22] temperature,[23] and illumination.[24] However, it is only recent that Lim et al chose a ST-PSC to investigate device degradation.[25] In this study, iodide ion migration-induced de-doping of spiro-MeOTAD was suggested as the origin of performance degradation of MoO_3-based ST-PSCs at elevated temperatures (≈70 °C). However, it is still unclear if the ion migration occurring across the perovskite/HTL interface is the exclusive cause of degradation of ST-PSCs or whether a unique interface that forms only in ST-PSCs, i.e., HTL/MoO_3 interface, also plays a part in device degradation. Therefore, HTL/MoO_3 interface may be worth investigating for any interfacial degradation mechanisms to obtain a better understanding of the stability of ST-PSCs.

It is well known that Spiro-MeOTAD HTL should be doped with lithium bis(trifluoromethanesulfonyl)imide (LiTFSI) to improve the conductivity.[26] It has been reported that, upon air exposure, Spiro-MeOTAD is oxidized (p-doped) along with concomitant formation of a byproduct namely Li_xO_y (Li_2O and/or Li_2O_2) which is converted from LiTFSI.[27] Thus, many groups include an intentional aerial oxidation step after HTL coating that lasts between a few hours and overnight.[28–31] The highly mobile and reactive Li-ions (Li^+) in the HTL has been known to greatly affect the performance and stability of conventional opaque PSCs.[32] For example, optimal diffusion of Li ions towards the ETL was reported to be beneficial for performance whereas an excess diffusion was reported to degrade the device.[33] It was also reported that LiTFSI diffuse towards the surface of the HTL as well during air-oxidation, resulting in a LiTFSI-dominated HTL surface.[34] For ST-PSCs, in particular, this LiTFSI-dominated HTL surface is in direct contact with MoO_3, which has been used as an electrode for lithium intercalation in the lithium-ion-battery field.[35–39] Thus, in addition to the previously known effects of Li-ion in the opaque PSCs, its effect on MoO_3-based ST-PSCs may be even more pronounced due to the highly reactive nature of Li ions with MoO_3, however, it remains unexplored. Unlike reactive and mobile Li ions, the concomitantly formed Li_xO_y (vide supra) on the HTL surface may interact with MoO_3 in a different way due to their relatively stable and immobile nature therefore they may be expected to have different effects on the performance and stability of ST-PSCs which are worth exploring.

Thus, in this work, we investigate the issue of low performance (low FF) and long-term stability of ST-PSCs based on an interfacial reaction possibly occurring at LiTFSI doped Spiro-MeOTAD HTL/MoO_3 interface. We found that LiTFSI dominated HTL surface resulting from the migration of LiTFSI during the conventional HTL oxidation (3 h aerial HTL oxidation is widely practiced for making opaque devices with Au back contacts which yield high FF exceeding 80% and good device stability) resulted in ST-PSCs with low initial PCE and rapid degradation during device aging, owing mainly to the inferior FF and its continuous drop with device aging, respectively. It was revealed that the Li ions dissociate from the LiTFSI dopant and start to diffuse into the MoO_3 buffer layer during the MoO_3 deposition and continue to diffuse for 400 h of device aging. This Li-ion diffusion

M. Keum, S. Kim
Solar Group
Jusung Engineering
Yongin 17094, Republic of Korea
A. Lambertz, K. Ding, W. Duan
IEK5-Photovoltaik
Forschungszentrum Jülich
52425 Jülich, Germany
E-mail: w.duan@fz-juelich.de

into MoO_3 causes a continuous drop in work-function (WF) of MoO_3 and a corresponding increase in the hole-injection barrier (HIB) at the HTL/MoO_3 interface which does not occur at the HTL/Au interface in opaque PSCs. Thus, ST-PSCs exhibited lower initial PCEs and FFs than their corresponding opaque PSCs, as well as fast device degradation due to the continuous drop in FF. In contrast, when the reactive LiTFSI at the HTL surface was converted into stable lithium oxides (Li_2O and/or Li_2O_2) via prolonged oxidation process, both the initial PCE and device stability of the ST-PSCs greatly improved due to effective mitigation of Li ion diffusion into MoO_3 at the HTL/MoO_3 interface. The distinguished aspect of this work is that it has unraveled the LiTFSI dopant-induced internal degradation mechanism unique to the ST-PSCs employing HTL/MoO_3/TCO structure. This work emphasizes that the reported internal degradation mechanisms remain at play even in the absence of external stimulus such as previously reported moisture-induced degradation of perovskite absorber layer caused by hygroscopic LiTFSI. The stable Li_xO_y successfully blocked the diffusion of Li^+ (from HTL) into interfacial MoO_3, thereby enabling a high PCE of 22.02% (21.68% certified), with a high FF (80.1%) and >99% storage stability for 400 h and >99% operational stability for 240 h. The improved ST-PSCs technology was further adopted to fabricate bifacial perovskite/silicon (Si) tandem solar cells, which exhibited bifacial equivalent efficiencies of 31.5% and 26.34% for four and two-terminal devices, respectively, at 20% albedo.

2. Results and Discussion

2.1. HTL Surface Modification

This work focuses on investigating the role of different lithium species dominating the HTL surface which are in direct contact with the MoO_3 buffer layer in ST-PSCs. It has been reported in the literature that LiTFSI migrates towards the HTL surface, particularly for higher LiTFSI doping contents (≈23 mol% of Spiro-MeOTAD), during the 3 hours of air exposure after spin-coating the HTL.[40] Due to the high optimum LiTFSI doping content (≈53 mol % of Spiro-MeOTAD) used in the HTL in this work,[41,42] we expect that our HTL surface has a large amount of LiTFSI as we will show later. To convert the Li ions from LiTFSI present at the HTL surface, we intentionally oxidized the HTL in controlled humidity (relative humidity [RH] ~10%) for varying periods of times. It has been reported in the literature that the oxidation of Spiro-MeOTAD results in concomitant formation of lithium oxides as explained by the following equations:[27]

$$\text{Spiro-MeOTAD} + O_2 \rightarrow \text{Spiro-MeOTAD}^+O_2^- \quad (1)$$

$$\text{Spiro-MeOTAD}^+O_2^- + Li^+TFSI^- \rightarrow \text{Spiro-MeOTAD}^+TFSI^- + Li_xO_y \quad (2)$$

The direct dependence of Li_xO_y formation upon spiro-MeOTAD's oxidation *(Vide supra)* enables us to control the conversion of Li ions to Li_xO_y on the HTL surface by manipulating the content of oxidized spiro-MeOTAD in the HTL. Although the oxidation of Spiro-MeOTAD HTL enables us to exploit the beneficial p-doping effect, however, we primarily focused on taking advantage of the generally overlooked phenomenon of concomitant Li_xO_y formation during the HTL oxidation step. The main motivation behind this is to investigate the effect of converting LiTFSI dominant HTL surface (i.e., rich in reactive Li ions) into a stable Li_xO_y-covered HTL surface on the charge transport behaviour and stability of the HTL/MoO_3 interface in ST-PSCs.

To achieve concomitant Li_xO_y formation on the HTL surface, we oxidized Spiro-MeOTAD HTL for various durations and measured their corresponding ultraviolet-visible (UV-Vis) absorptance spectra as shown in **Figure 1**a. We found that increasing the oxidation duration of HTL resulted in an increase in peak intensity at 521 nm corresponding to the oxidized Spiro-MeOTAD. We quantified the oxidized Spiro-MeOTAD content from the UV-Vis absorptance spectra according to the protocol reported by Rebecka et al.[43] Briefly, we used the ratio of the absorptance peak intensity at 521 nm (which pertains to oxidized Spiro-MeOTAD) to the absorptance peak intensity at the pseudo-isosbestic point at ≈407 nm to form a standardized absorptance ratio (SAR). The SAR value shows the amount of oxidized Sprio-MeOTAD present in the film. The 3 hours oxidized Spiro-MeOTAD HTL (hereafter referred to as control HTL) showed an oxidized Spiro-MeOTAD content of 2.21% whereas, 4 days oxidized Spiro-MeOTAD HTL (hereafter referred to as target HTL) showed the highest peak at 521 nm with oxidized spiro-MeOTAD content calculated to be 6.14% as shown in Table S3, Supporting Information. This shows 2.78 times increase in the content of oxidized Spiro-MeOTAD during the said oxidation duration which also causes the concomitant formation of Li_xO_y at the target HTL surface as per the oxidation mechanism of Spiro-MeOTAD expressed by Equations 1 and 2.

To verify the different surface dominating species (LiTFSI and Li_xO_y) on control and target HTL surfaces, we carried out X-ray photoelectron spectroscopy (XPS) measurements of both control and target HTL surfaces as shown in Figure S1, Supporting Information. In the case of control HTL, a prominent peak corresponding to the Li cation in LiTFSI in Li1s spectra as well as evidence of TFSI anion in LiTFSI was observed in the form of signals corresponding to the CF_3 groups in the high binding energy (BE) C1s (BE = 293 eV) and F1s peaks, sulfonamide groups doublet (BE = 169, 170.1 eV) in S2p spectra and negatively charged nitrogen of the TFSI anion in N1s peak (BE = 399.5 eV).[44] This suggests that the control HTL surface is dominated by LiTFSI that diffused during 3 h HTL oxidation. On the other hand, the F 1s and S 2p spectra showed a reduction in peak intensity for the target HTL relative to the control HTL (Figure S1d,e, Supporting Information), indicating that LiTFSI may not be the surface dominant specie in the target HTL. This change was accompanied by a clear strengthening of the O 1s signal near 532 eV, which corresponds to oxygen in Li_xO_y (Li_2O and/or Li_2O_2) (Figure S1c).[27] The deconvoluted O 1s spectra in Figure 1b,c indicate considerably large formation of Li_xO_y on the target HTL surface as compared to the control HTL surface.

The distinct surface-dominating species in control and target HTLs were further revealed by comparing their surface energy properties. The static water contact angles of 66.49° and 57.32° were measured for control and target HTLs, respectively (Figure 1d,e). A lower static water contact angle for target HTL indicates a relatively higher surface energy, likely because Li_xO_y dominated its surface. We used density-functional theory (DFT)

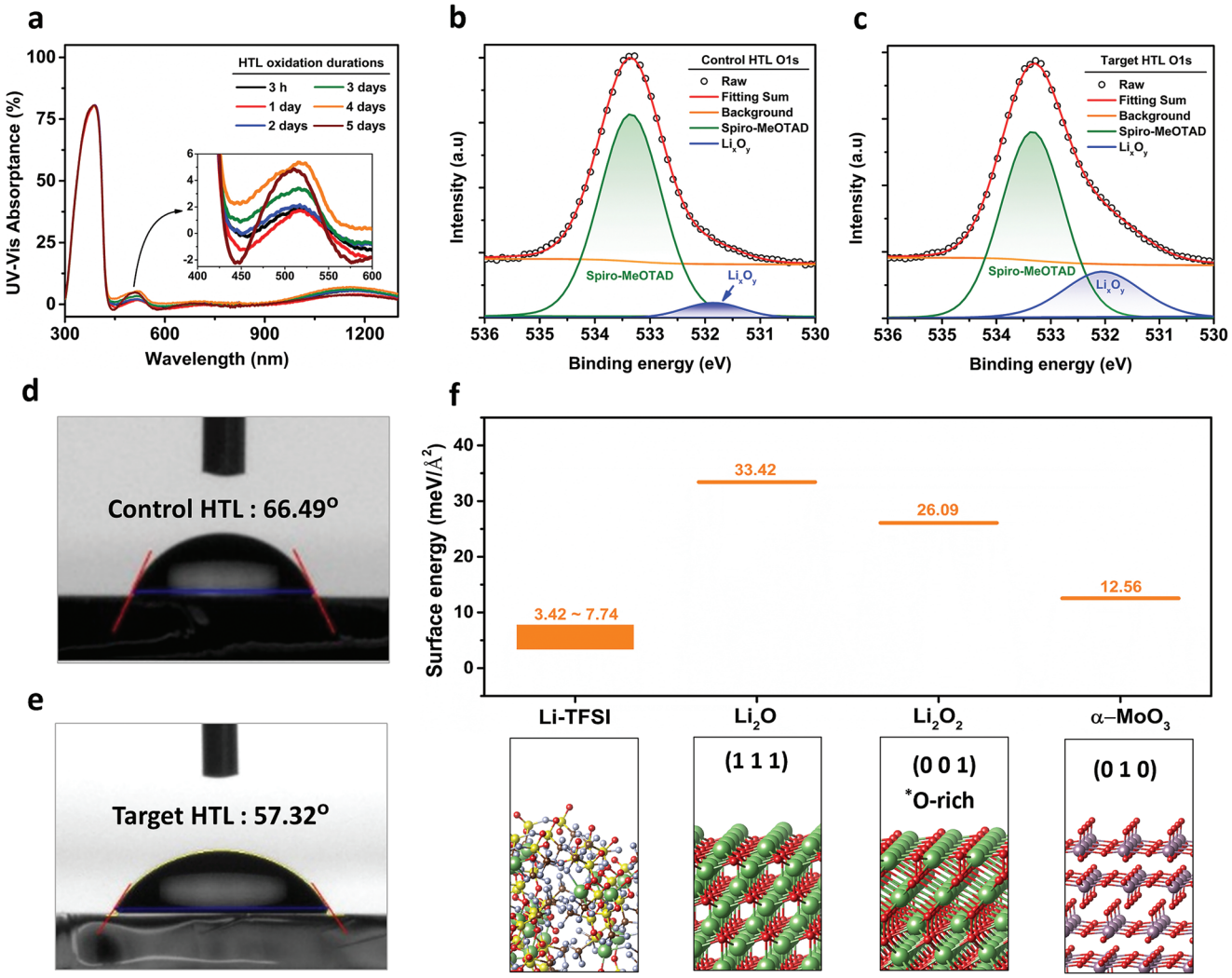

Figure 1. a) UV-Vis absorptance spectra of Spiro-MeOTAD HTL after various oxidation durations. Deconvoluted XPS O1s spectra of b) control HTL and c) target HTL. Static contact angle measurements of d) control HTL and e) target HTL. f) DFT calculated surface energies and atomic structures of LiTFSI, Li_2O, Li_2O_2, and α-MoO_3.

to calculate the surface energy values of LiTFSI, Li_xO_y (Li_2O and Li_2O_2) and α-MoO_3. The atomic structures of species used in DFT calculations are given in Figure S2, Supporting Information and details of this and subsequent mentions of DFT computations are given in supplementary information. As shown in Figure 1f, the calculated surface energy value of LiTFSI (surface dominant specie in control HTL) was 3.42 to 7.74 meV/Å^2 and that of Li_2O and Li_2O_2 (surface dominant species in target HTL) were 33.42 meV/Å^2 and 26.09 meV/Å^2 respectively. The different surface energy values of surface dominating species in control and target HTLs relative to α-MoO_3 (which was calculated to be 12.56 meV/Å^2) even led to different initial growth modes of MoO_3. The scanning electron microscopy (SEM) images of thermally evaporated MoO_3 film (1.2 nm in thickness) on the control and target HTL surfaces are shown in Figure S3a,d, Supporting Information. The lower surface energy value of LiTFSI relative to MoO_3 resulted in an island growth of MoO_3 on the control HTL surface (Figure S3a, Supporting Information) whereas the higher surface energies of Li_2O and Li_2O_2 relative to MoO_3 enabled a uniform growth of MoO_3 on the target HTL surface (Figure S3d, Supporting Information). This clearly reveals that HTL surface modification with Li_xO_y was achieved for the entire area of the target HTL samples via controlled HTL oxidation. It may be noted that although the initial growth mode of MoO_3 on control HTL is island-like, the SEM image of thicker MoO_3 deposition (12 nm) (Figure S3c, Supporting Information) shows that the MoO_3 islands apparently disappear at MoO_3 thickness of 12 nm.

2.2. Effect of HTL Surface Modification on Performance and Stability of Opaque and ST-PSCs

The above results confirmed the HTL surface modification from LiTFSI-dominated surface to Li_xO_y-dominated surface via excess aerial oxidation of the HTL. Next, we investigated the effects of the HTL surface modification on the photovoltaic

Table 1. Photovoltaic parameters of opaque and ST-PSCs constructed with control and target HTLs before and after device aging. The tabulated values have been averaged from the reverse and forward *J–V* scans.

Samples	Opaque PSCs				ST-PSCs			
	J_{sc} (mA cm^{-2})	V_{oc} (V)	FF	PCE (%)	J_{sc} (mA cm^{-2})	V_{oc} (V)	FF	PCE (%)
Control fresh	23.96	1.059	0.697	17.69	22.64	1.081	0.738	18.07
Control aged	23.47	1.132	0.821	21.82	22.28	1.022	0.395	8.98
Target fresh	23.29	1.104	0.810	20.83	22.67	1.107	0.801	20.11
Target aged	23.39	1.130	0.824	21.77	22.69	1.096	0.802	19.95

performance and stability of both opaque and ST-PSCs. **Figure 2**a,b show the photographs of working opaque and ST-PSC devices respectively, whereas Figure 2c shows the transparency of a perovskite filter made exactly as ST-PSC without the Au contact deposition. The device structures of opaque and ST-PSCs used in this study are illustrated in Figure 2d,e respectively. Figures S4 and S5, Supporting Information show current density-voltage (*J–V*) curves of opaque and ST-PSC devices, respectively, fabricated using HTLs that underwent various oxidation durations (i.e., with varying contents of Li_xO_y on the surface), which were intermittently measured during 400 h of device aging. The device aging throughout this manuscript refers to the aging of unencapsulated devices in dark conditions with controlled RH of ≈10% at room temperature. The corresponding photovoltaic parameters are given in Table S4, Supporting Information. Representative data from Figures S4 and S5 and Table S4, Supporting Information are presented in Figure 2g–i and **Table 1** where "fresh" indicates *J–V* measurement right after device fabrication and "aged" indicates *J–V* measurement after 400 h of device aging.

Regardless of the HTL oxidation duration, opaque PSCs achieve decent PCEs (21%–22%), with no degradation after 400 h of device aging (Figure 2g,i and Table 1). However, ST-PSCs fabricated with control HTL (control ST-PSCs) had low initial PCE values (18.07%), which dropped down to 8.98% during 400 h of device aging (Figure 2h and i and Table 1), driven by the lower initial FF of 74% and its corresponding reduction to 40%, respectively. In contrast, ST-PSCs fabricated with target HTLs (target ST-PSCs) exhibited higher initial PCEs (20.11%) and retained >99% of the initial PCE after 400 h of device aging. The impressive shelf stability of the target ST-PSCs was driven by their high initial FF of more than 80%, which was well preserved for 400 h of device aging. A statistical data showing the differences in *J–V* parameters of 42 control and target ST-PSC devices before and after device aging is given in Figure 2f showing that the formation of Li_xO_y on HTL surface not only improves the PCE and stability of best devices but also reduces performance variation across several batches of devices.

The low initial FF and the subsequent drop in FF during device aging were only observed in control ST-PSCs and not in control opaque PSCs, which suggests that the degradation in control ST-PSCs most likely occurs at the HTL/MoO_3 interface. This claim was further supported by the following two experiments. In the first test, it was checked if the reason for the degradation of control ST-PSCs is the degradation of perovskite absorber layer. A sufficiently degraded control ST-PSC (over 400 h device aging) was subjected to removal of IZO electrodes, and the underlying MoO_3 buffer layer followed by washing-off the HTL by dropping chlorobenzene while spinning at 3000 rpm for 30 s. This resulted in revealing the perovskite absorber surface as illustrated in Figure S6, Supporting Information. Afterward, a new HTL was spin-coated and exposed to 3 h of aerial oxidation (same as the control condition). A 12 nm MoO_3 buffer layer followed by IZO was redeposited in the same manner as explained in the *"Fabrication of ST-PSCs"* section. The so recovered ST-PSC showed a similar *J–V* curve as the control ST-PSC before the degradation as shown in Figure 2j. It proves that the perovskite absorber did not get affected by the device degradation occurred during device aging. Figure S7, Supporting Information shows the XRD spectra of fresh perovskite film as well as the perovskite film of a degraded ST-PSC device after removing HTL/MoO_3/IZO layers. The XRD spectra of the perovskite film after device degradation shows no noticeable signs of perovskite film degradation. In the second test, the stability of the MoO_3/IZO structure was tested by evaporating a 12 nm MoO_3 layer on an ITO substrate followed by sputtering of IZO electrode on top of MoO_3 as shown in Figure S8a, Supporting Information. The current-voltage (*I–V*) scans were performed right after fabricating this device and then again after a device aging for 400 h as shown in Figure S8b, Supporting Information. No observable difference in *I–V* curves was found due to device aging suggesting that the MoO_3/IZO structure does not degrade with device aging. These results confirm the HTL/MoO_3 interface to be the most probable location for the degradation to take place.

Figure 2i revealed that the degradation at the HTL/MoO_3 interface was mitigated by the formation of Li_xO_y on the HTL surface in target ST-PSCs (i.e., following 4-day oxidation of the HTL). However, it is also necessary to consider the effects of other changes in the HTL that simultaneously occurred during the oxidation duration before we firmly establish the positive role of Li_xO_y. Two important aspects of HTL oxidation process need investigation in this regard. First aspect to test is whether a simple delay after HTL coating and before MoO_3 buffer layer deposition instead of the oxidation process is related to the observed improvement in the target ST-PSCs performance. This was tested by exposing the HTL to pure nitrogen (N_2) environment for 4 days after initial 3 h ambient air exposure (to ensure the initial LiTFSI migration towards the surface same as control HTL). As shown in Figure S9, Supporting Information, the ST-PSC constructed with the N_2-exposed HTL showed inferior performance and poor stability resembling that of control HTL thus proving that the oxidation was the key for the observed

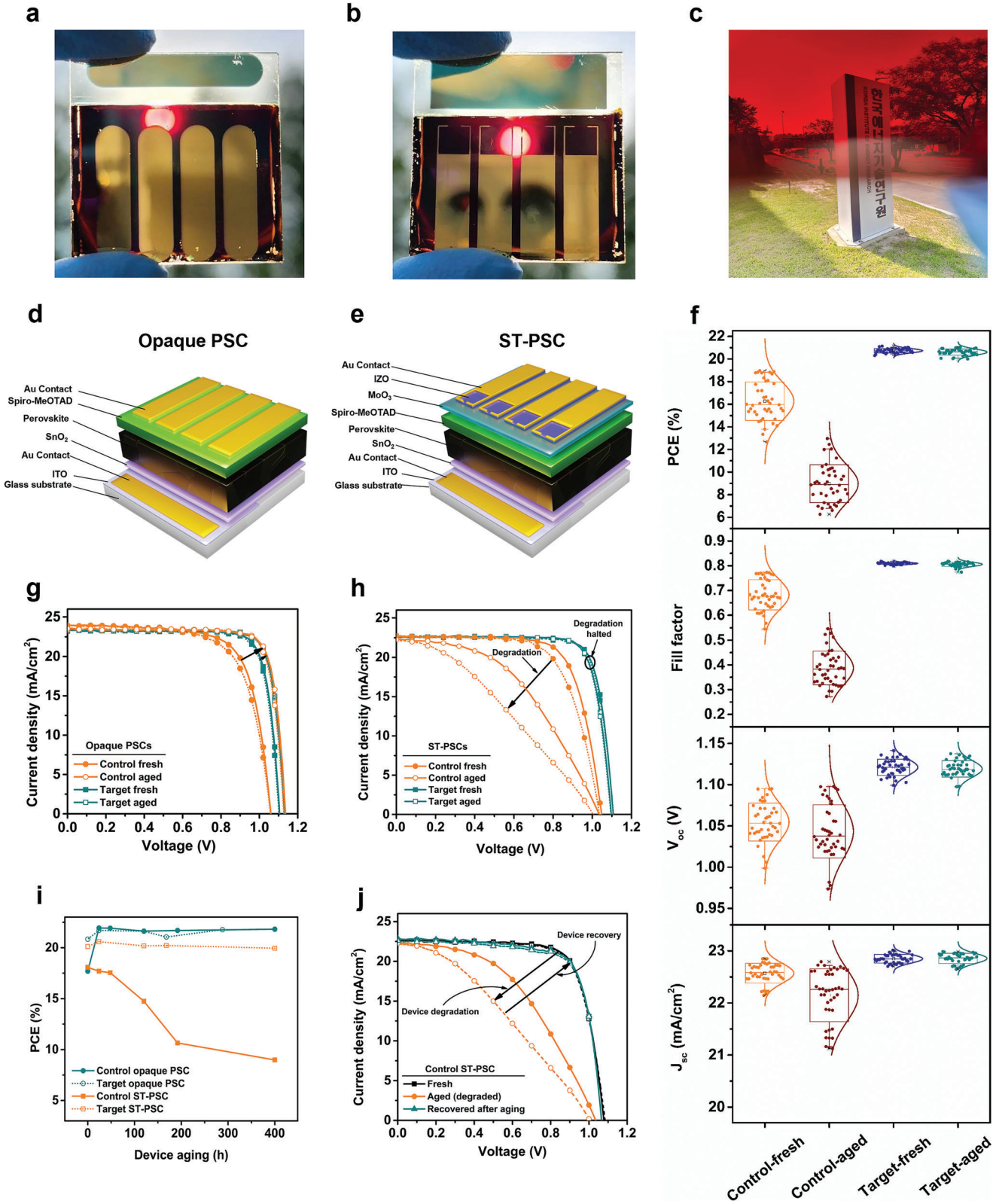

Figure 2. Photographs of an a) opaque PSC, b) ST-PSC, and c) perovskite top cell filter. Device structure of an (d) opaque PSC and e) ST-PSC. f) Statistical distribution of photovoltaic parameters including J_{SC}, V_{OC}, FF, and PCE of 42 control and target ST-PSC devices before and after device aging. *J–V* curves of fresh and aged g) opaque PSCs and h) ST-PSCs constructed with control and target HTLs. i) Effect of device aging on PCE of opaque and ST-PSCs constructed with control and target HTLs. j) *J–V* curves of a control ST-PSC before and after degradation and after recovery by redeposition of HTL/MoO_3/IZO layers. Solid and dashed lines in *J–V* curves represent reverse and forward *J–V* scans, respectively.

improvements. The second aspect requiring clarity is whether the enhanced performance and stability of target ST-PSC is a consequence of the target HTL's higher doping level (i.e., higher oxidized Spiro-MeOTAD content) instead of the formation of Li_xO_y at its surface. To investigate this aspect, tris(2-(1H-pyrazol-1-yl)−4-tert-butylpyridine)cobalt(III) tri[hexafluorophosphate] commonly called FK209 Co(III) PF_6 salt or simply FK209 has been used as dopant along with LiTFSI to achieve instant oxidation of Spiro-MeOTAD in solution which is then spin-coated in pre-oxidized form without the need of extended oxidation time post spin-coating, thus eliminating the possibility of large formation of Li_xO_y on the HTL surface. In this way, isolated effect of higher Spiro-MeOTAD$^+$ content can be studied. UV-Vis absorptance spectra of the (4 day oxidized) target HTL and FK209 doped HTL shown in Figure S10a, Supporting Information confirm that the FK209 doped spiro-MeOTAD instantly achieves a similar level of oxidation as target HTL. A comparison of XPS O1s spectra for control, target, and FK209 doped HTLs is given in Figure S10b, Supporting Information which shows great similarity between FK209 doped HTL and control HTL. A deconvoluted O1s spectra shown in Figure S10c, Supporting Information further confirms that FK209 doped HTL surface has only a small signal from Li_xO_y which resembles the Li_xO_y signal in control HTL (Figure 1b) and is much smaller as compared to the Li_xO_y signal in target HTL (Figure 1c). This confirms that the FK209 doping of HTL only achieves a higher doping content without forming large amount of Li_xO_y on its surface. Reference opaque devices using FK209 doped HTL were fabricated to confirm that the FK209 doped Spiro-MeOTAD HTL recipe used is well optimized. A high PCE of ≈21.5% as well as a decent shelf stability was observed for the opaque PSCs built with FK209 doped HTL as shown in Figure S10d,e and Table S5, Supporting Information. Next, ST-PSCs employing the FK209 doped HTL were fabricated which showed low initial PCE relative to the target ST-PSCs as well as accelerated degradation as shown in Figure S10d,f and Table S5, Supporting Information. This confirms that the increase in oxidized Spiro-MeOTAD content itself in target HTL was not correlated with the observed improvements in performance and stability of the target ST-PSCs thus firmly establishing that the formation of Li_xO_y on the target HTL surface was indeed crucial for the enhanced performance and stability of the target ST-PSCs.

2.3. Interfacial Degradation Mechanism and its Mitigation at HTL/MoO_3 Interface

Next, we focused on determining the reason behind the low PCE and fast degradation of control ST-PSCs and exploring how the HTL surface modification with Li_xO_y can enhance the PCE and device stability. As mentioned earlier, the Li-ion is known to intercalate into MoO_3 in lithium-ion-batteries field.[38,39] This motivated us to investigate the possible interaction of Li ions with the MoO_3 at the HTL/ MoO_3 interface, its effects on the interfacial degradation and charge transport characteristics. For investigating the interaction of Li ions with MoO_3 at the HTL/MoO_3 interface, we performed time-of-flight secondary ion mass spectroscopy (TOF-SIMS) analysis on aged (400 h) control and target ST-PSCs samples as shown in **Figure 3a**. The Li^+ profile in control ST-PSC shows a higher intensity and is detected deeper within the MoO_3 layer as evident by the larger overlap with the Mo^+ profile as compared to that in target ST-PSC. This suggests that the Li^+ from LiTFSI in the control sample can readily diffuse into MoO_3 as illustrated in Figure S11b, Supporting Information (left). However, the Li^+ profile in target ST-PSC has shown a lower intensity, detected farther away from the MoO_3 layer and closer to the HTL as compared to control ST-PSC which suggests that the Li^+ signal in target ST-PSC is coming from the Li_xO_y at the target HTL surface and Li diffusion into the MoO_3 layer has been blocked by the Li_xO_y as illustrated in Figure S11c, Supporting Information (right). The differences in Li^+ profiles between control and target ST-PSCs at the HTL/MoO_3 interface are better observed in linear scale plot of Li^+ and Mo^+ profiles given in Figure S11a, Supporting Information. It may be noticed that the Li^+ profile in the target ST-PSC also appears to slightly overlap with the Mo^+ profile. This may be attributed to the matrix effect commonly observed in TOF-SIMS measurements which manifests itself at interfaces. The matrix effect is essentially premature detection of an element (in this case Li^+) located underneath another element (in this case Mo^+) due to the ionization process. Therefore, it can be concluded that the Li^+ diffusion into MoO_3 is effectively mitigated by Li_xO_y in target ST-PSCs.

The role of surface dominating species (LiTFSI in control HTL and Li_xO_y in target HTL) in different Li diffusion patterns into the interfacial MoO_3 observed in TOF-SIMS analysis of the control and target ST-PSCs was further investigated by DFT calculations. In control ST-PSCs, since the HTL surface is dominated by LiTFSI, therefore Li^+ diffusion into interfacial MoO_3 should consist of three steps: (i) Li^+ dissociation from LiTFSI at the HTL surface, (ii) Li interstitial (Li_i) formation in MoO_3 (Li intercalation at the surface) and (iii) migration of Li^+ through MoO_3 lattice. DFT computations revealed a negative dissociation energy of LiTFSI (Figure S12, Supporting Information), a negative and small Li_i formation energy in MoO_3 (based on the structure shown in Figure 3b (left)) under Mo- and O-rich MoO_3 conditions, respectively, as shown in Figure 3b (right), revealing that Li intercalation into MoO_3 at the interface is highly likely in the control sample. In addition, the lowest Li migration barrier into MoO_3 is found to be 0.433 eV as shown in Figure S13b, Supporting Information. This value is comparable with the Li diffusion barrier (0.2– 0.7 eV) in the graphite anode of a Li-ion battery,[45] suggesting a slow but clear Li diffusion in the investigated control ST-PSCs consistent with the TOF-SIMS analysis. On the other hand, the target HTL surface is covered with Li_xO_y (Li_2O and/or Li_2O_2), therefore Li intercalation into MoO_3 in target ST-PSC may occur only if Li_xO_y: (i) eject Li^+ from within their lattice or (ii) diffuse Li^+ provided by the LiTFSI present in the underlying HTL. Therefore, Li^+ diffusion into MoO_3 is possible only if Li^+ transport channel such as Li vacancies (V_{Li}), Li interstitials (Li_i), and/or Frenkel (V_{Li}-Li_i) defects form in the lattice of Li_xO_y. Therefore, we used DFT to calculate the formation eneries and concentration of V_{Li}, Li_i, and Frenkel (V_{Li}-Li_i) defects in Li_2O and Li_2O_2 at 300 K under the oxygen partial pressure of 0.2 atm (air condition). The calculated V_{Li}, Li_i, and Frenkel (V_{Li}-Li_i) defect structures in Li_2O and Li_2O_2 are depicted in Figure S14, Supporting Information and their formation energies and concentrations at 300K are tabulated in Table S6, Supporting Information. Figure 3c shows that, at the atmospheric oxidation condition, the formation energy of

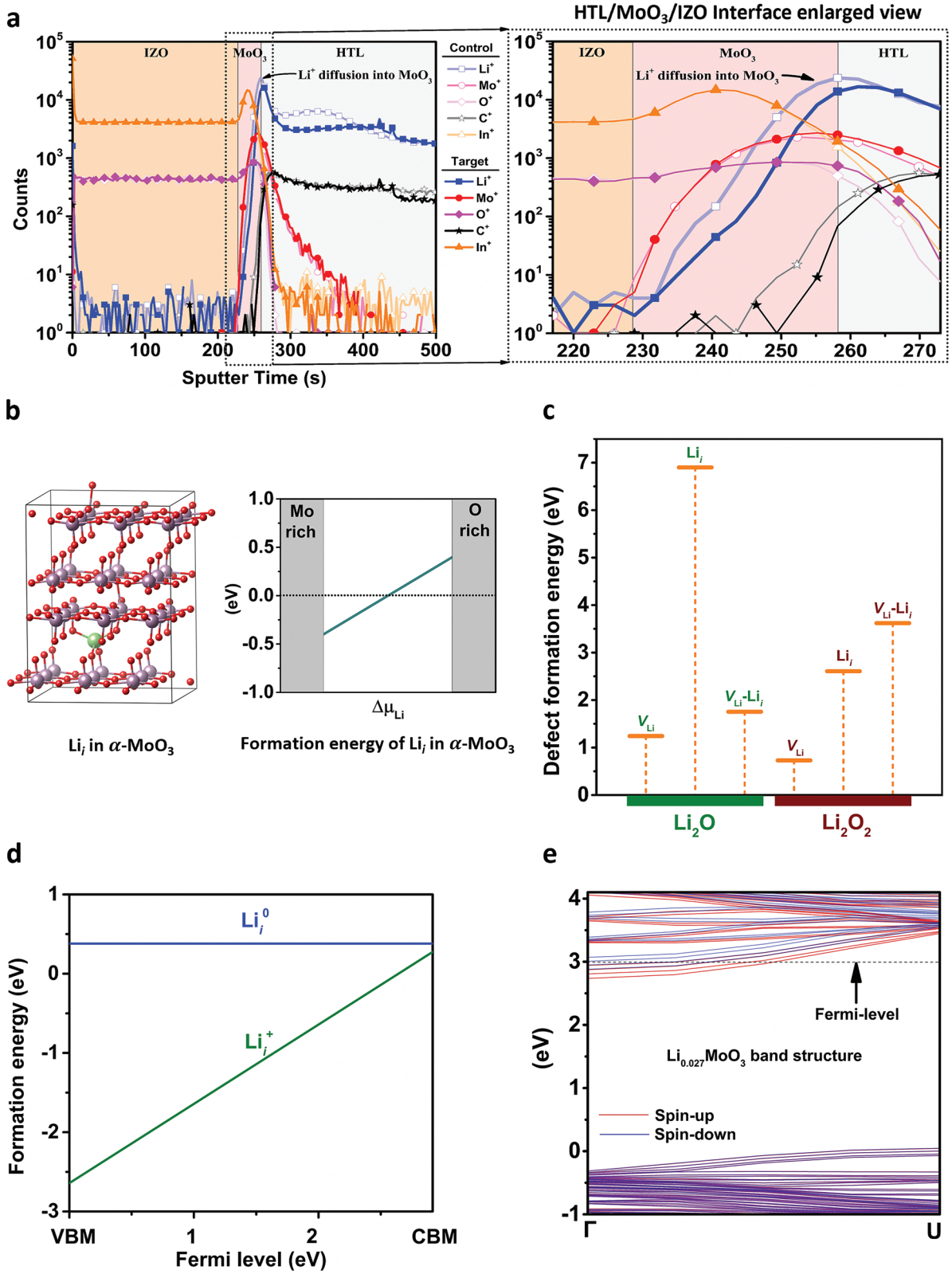

Figure 3. a) TOF-SIMS analysis of Li^+ diffusion across the HTL/MoO_3 interface in control and target ST-PSCs (left) and enlarged view of HTL/MoO_3/IZO interface (right). b) Atomic structure of α-MoO_3 with Li interstitial (Li_i) (left), and formation energy of Li_i in MoO_3 with respect to Li chemical potential (right). c) Li vacancy (V_{Li}), Li interstitial (Li_i), and Frenkel (V_{Li}- Li_i) defect formation energies in Li_2O and Li_2O_2. d) Formation energy plot of charged Li_i defect and corresponding +/0 transition level. e) The band structure of MoO_3 with Li_i ($Li_{0.027}MoO_3$) showing WF reduction.

aforementioned defects is generally high (>1 eV) in both the Li_2O and Li_2O_2, suggesting that Li^+ diffusion into MoO_3 is highly unlikely when target HTL surface is dominated by Li_xO_y. One exception is the case of V_{Li} in Li_2O_2 with a formation energy of 0.73 eV, however, even in this case the positive defect formation energy in contrast to the negative Li^+ dissociation energy from LiTFSI (indicating spontaneous Li^+ supply) in control ST-PSCs strongly supports the observed differences in the diffusion behavior of Li ions between the control and target ST-PSCs in the TOF-SIMS results.

The Li^+ diffusion into MoO_3 in control ST-PSCs and its effective blocking in target ST-PSCs requires an investigation of the effects of Li^+ inclusion into MoO_3 on the electrical properties of the latter. The DFT calculations revealed a shallow donor-like nature of Li_i^+ in MoO_3 (Figure 3d) which can reduce the work-function (WF) of MoO_3 as shown in Figure 3e. These DFT computations (details of DFT computations are available in the supplementary information) establish a connection between the Li^+ diffusion (as observed in control ST-PSCs) and work-function (WF) reduction of MoO_3 at the control HTL/MoO_3 interface. It also implies that the effective blocking of Li^+ diffusion into MoO_3 as observed in target ST-PSCs results in preservation of MoO_3 WF in the target ST-PSCs.

The Li^+ diffusion-induced work function reduction of MoO_3 at the HTL/MoO_3 interface in control ST-PSC needs to be considered for its effects on the energetics of this interface because WF of a metal-oxide layer interfacing an organic semiconductor (OS) is known to play a crucial role in determining the interfacial charge transport behavior. The energetics of metal oxides and OS interfaces is governed by the universal energy alignment rule,[46] which states that the HOMO of the OS is pinned to the fermi level (E_f) of metal oxide maintaining a minimum offset when the ionization energy (IE) of the OS equals the WF of the metal oxide. From this point, further increase in WF of metal oxide does not reduce the offset of HOMO pinning towards E_f however a drop in WF will contribute to a corresponding increase in the offset of HOMO pinning. To understand the consequences of this universal energy alignment rule for the charge transport at HTL/MoO_3 interface (in view of an OS and metal oxide interface), schematic illustration of hole-extraction from the HTL as well as hole-injection into the HTL are presented in **Figure 4**a,b, respectively. As shown in Figure 4a, the hole extraction from the HTL takes place via an electron transfer from the conduction band (CB) of the MoO_3 to the HOMO of the HTL whereas the hole injection takes place via electron transfer from HOMO of HTL to the CB of MoO_3 as shown in Figure 4b.[47,48] In the case of hole-injection the offset of HTL HOMO below the E_f acts as a barrier for electron transfer from the HTL HOMO to the CB of MoO_3 (Figure 4b) therefore this offset is termed as hole-injection barrier (HIB). A small HIB pins the HTL HOMO towards the E_f maintaining a small offset thus enabling a favorable charge transfer as shown in Figure 4b whereas a large HIB (depending upon the relative difference of IE of HTL and WF of MoO_3 as described above) may pin the HTL HOMO away from the E_f as shown in Figure 4c. In such a band alignment at HTL/MoO_3 interface (Figure 4c) the large HIB hinders the hole-injection which resists the diffusion current in solar cell whereas the downward pinning of HTL HOMO (away from the E_f) near the HTL/MoO_3 interface makes the transport of holes from the bulk of HTL towards the HTL/MoO_3 interface unfavorable as well, thus creating a double-sided hole transport barrier. It was reported that the shape of the *J-V* curves is slightly affected in the form of apparent increase in series resistance (causing reduction in FF) when the HIB is not substantially large, whereas a large HIB manifests itself in the form of S-shaped *J–V* curves.[49] We also observed in Figure S5a, Supporting Information that our control ST-PSCs start to degrade in the form of an apparent increase in series resistance (causing a reduction in FF) at initial stages of device degradation but the *J–V* curve eventually appears as an S-shape *J–V* curve after sufficient degradation of the control ST-PSC as shown in Figure S15, Supporting Information. This strongly suggests the presence of an evolving HIB in control ST-PSCs caused by WF reduction of MoO_3 due to the observed Li^+ diffusion into the MoO_3, as described by the DFT computations and TOF-SIMS analysis respectively.

The evolving HIB characteristics at the HTL/MoO_3 interface in control ST-PSCs were experimentally verified by investigating the aging-dependent changes in band alignment at the HTL/MoO_3 interface for the control and target samples via ultraviolet photoelectron spectroscopy (UPS). For this, we first optimized the thickness of the MoO_3 layer for acquiring a clear signal from the underlying HTL to be 0.5 nm by its in situ deposition (Figure S16, Supporting Information). UPS measurements were then performed on the control and target HTL/MoO_3 samples twice. The first measurements (termed as fresh) were made immediately after the in situ MoO_3 deposition on HTL samples, and the second measurements (termed as aged) were performed after aging the HTL/MoO_3 samples for 170 h in the ultrahigh vacuum chamber of the UPS measurement apparatus. The WF and HOMO pinning offset (i.e., HIB) at the HTL/MoO_3 interfaces in both control and target samples were extracted from the UPS spectra and presented in Figure 4d,e, respectively. It is noticeable that for the fresh samples, an HIB of 0.78 eV and 0.67 eV was observed for the control and target samples, respectively, as shown in Figure 4f. Furthermore, after 170 h of aging, the HIB at HTL/MoO_3 in the control group increases to 1.18 eV, whereas it remains unchanged at 0.67 eV in target group (Figure 4f). These results are in excellent match with the observed trends of device performance with respect to device aging time, which was mainly driven by FF changes.

Reconsidering the universal energy alignment rule described earlier, the HIB in our case must be determined by the relative difference of IE of HTL and WF of MoO_3, therefore not only the WF of MoO_3 but a change in IE of HTL can also contribute to the increase in HIB observed in control ST-PSCs. For this reason, we checked the IE of HTL surface from the UPS data given in Figure 4d,e (by adding WF of HTL to HIB), and found that the IE of HTL remains similar (between 5.5 and 5.6 eV) in all the cases, suggesting that the IE of HTL does not cause the increase in HIB observed at HTL/MoO_3 interface in control ST-PSCs, therefore we can conclude that the WF of MoO_3 is the sole contributor to the HIB increase observed in control ST-PSC.

In addition, a large HIB of 1.18 eV observed for the aged control group may cause the downward band bending of HTL HOMO near the HTL/MoO_3 interface, considering that HOMO of a similarly oxidized spiro-MeOTAD was reported to lie at an E_f-HOMO offset of approximately 0.6 eV.[33] This downward band bending of HOMO may act as a hole-extraction barrier as shown

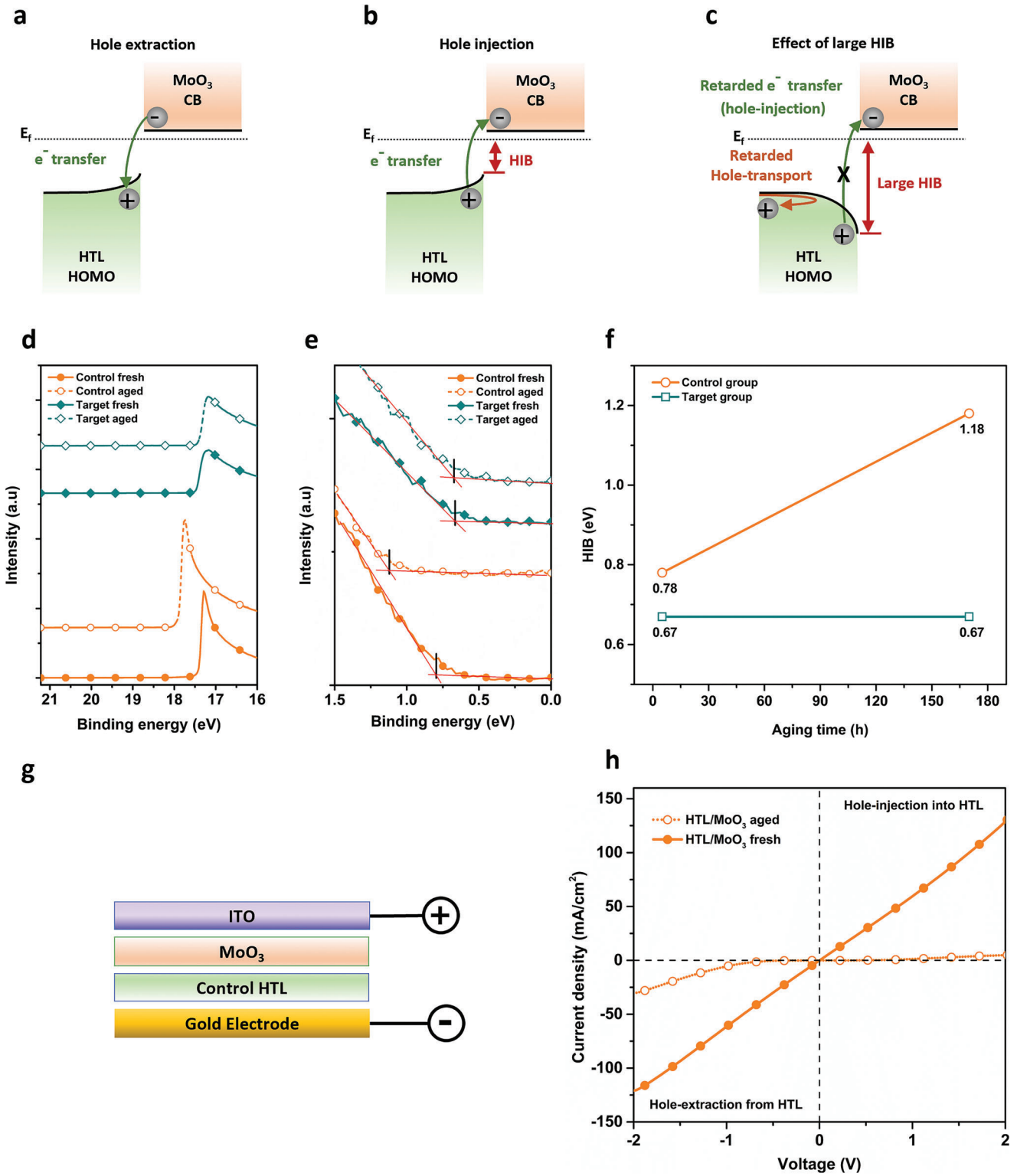

Figure 4. Illustration of HTL/MoO_3 interface band diagram showing a) hole extraction from the HTL and b) hole injection into the HTL. c) HTL/MoO_3 interface band alignment illustration showing effect of large HIB on charge transport/transfer across HTL/MoO_3 interface. UPS measurements showing d) work function and e) HOMO structure of HTL/MoO_3 interface for control and target samples before and after aging. f) Effect of device aging on HIB at HTL/MoO_3 interface for control and target samples. g) Device structure of hole only device containing the control HTL, and (h) *J–V* characteristics of the hole-only device with device aging.

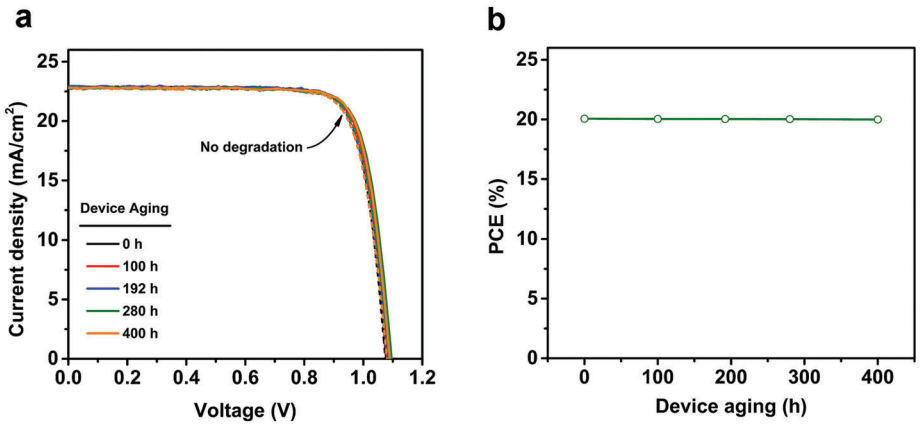

Figure 5. Effect of device aging on a) *J–V* curves and b) PCE of the ST-PSC made with pure O_2 oxidized HTL. Solid and dashed lines in *J–V* curves represent reverse and forward *J–V* scans, respectively.

in Figure 4c thus indicating the presence of a double-sided hole transport/transfer barrier. To directly test hole-transport across HTL/MoO_3 interface, a hole-only device containing the control HTL (Figure 4g) was constructed, and its electrical characteristics were investigated. The device initially shows an ohmic behavior whereas severe current blocking was observed after aging for 400 h. In particular, the asymmetric nature of the *J-V* curve of the aged device confirms the presence of the double-sided hole barrier,[50] in which a very high hole-injection barrier (into the HTL) with a relatively weaker barrier for hole extraction (from the HTL), both of which may explain the significant FF drop in the aged control ST-PSCs.

From all these experimental and computational data, it can be concluded that the inferior photovoltaic performance and its subsequent degradation in control ST-PSC is due to the higher HIB in fresh control ST-PSCs and its continuous increase with device aging, respectively, caused by the WF reduction of MoO_3 (due to the Li^+ diffusion into the MoO_3). In contrast, the small and unchanging HIB in target group results in the efficient and stable photovoltaic performance by preserving the WF of MoO_3 (via mitigating Li^+ diffusion into MoO_3).

2.4. Proof of HTL Surface Modification Concept with Practically Faster Oxidation

From our discussion, we have established that modifying the HTL surface by converting LiTFSI into stable Li_xO_y via an extensive oxidation of HTL significantly improves the performance and stability of ST-PSCs. However, extended oxidation duration (4 days for target HTL) needed for the above-mentioned improvements questions the practicality of this approach from a commercialization perspective. To address this issue together with reconfirming the viability of HTL surface modification strategy, we attempted to form stable Li_xO_y on the LiTFSI-dominated surface of control HTL via accelerated oxidation. Briefly, we subjected a control HTL (that has already undergone initial 3 h of air exposure) to a forced oxygen (O_2) flow for 4 hours expecting a swift formation of stable Li_xO_y on the HTL surface due to higher concentration of oxygen contacting the HTL surface as compared to oxidation in static air with controlled RH of ~10%. The initial 3 h of air exposure was intended to facilitate the migration of LiTFSI towards the HTL surface (consistent for all the conditions investigated in this work). After that, a pure O_2 forced flow was exploited to swiftly oxidize the surface LiTFSI only into stable Li_xO_y while halting further LiTFSI migration to the surface, based on the report that moisture is necessary for LiTFSI migration to the surface while there is no LiTFSI migration in pure O_2 environment.[51] **Figure 5**a,b and **Table 2** show that the ST-PSCs constructed using the HTL subjected to such an accelerated pure O_2 oxidation demonstrated an excellent PCE of 20.06%, > 99% of which was preserved after 400 h of device aging, reconfirming that the formation of surface Li_xO_y is crucial for the improved performance and stability of ST-PSCs. At the same time, it was successfully demonstrated that surface Li_xO_y can be formed in an accelerated manner compared to aerial oxidation addressing the practicality concerns by reducing the oxidation duration from 4 days down to 4 hours.

Table 2. Effect of device aging *J–V* parameters of ST-PSCs made with pure O_2 oxidized HTL. The values have been averaged from reverse and forward *J–V* scans.

Device aging (h)	J_{sc} (mA cm^{-2})	V_{oc} (V)	FF	PCE (%)
0	22.83	1.09	0.81	20.06
100	22.85	1.09	0.80	20.04
192	22.90	1.10	0.80	20.03
280	22.80	1.10	0.80	20.02
400	22.79	1.09	0.80	19.99

2.5. Champion ST-PSC and Tandem Device Characteristics

The champion target ST-PSC achieved a PCE of 22.02% with an FF higher than 80%. The *J-V* and external quantum efficiency (EQE) results of the champion device are presented in **Figure 6**a,b, respectively and device parameters are provided in **Table 3**. The certified *I-V* measurement results of champion ST-PSC showed a PCE of 21.68% as shown in Figure S17, Supporting Information. To the best of our knowledge, this is the highest

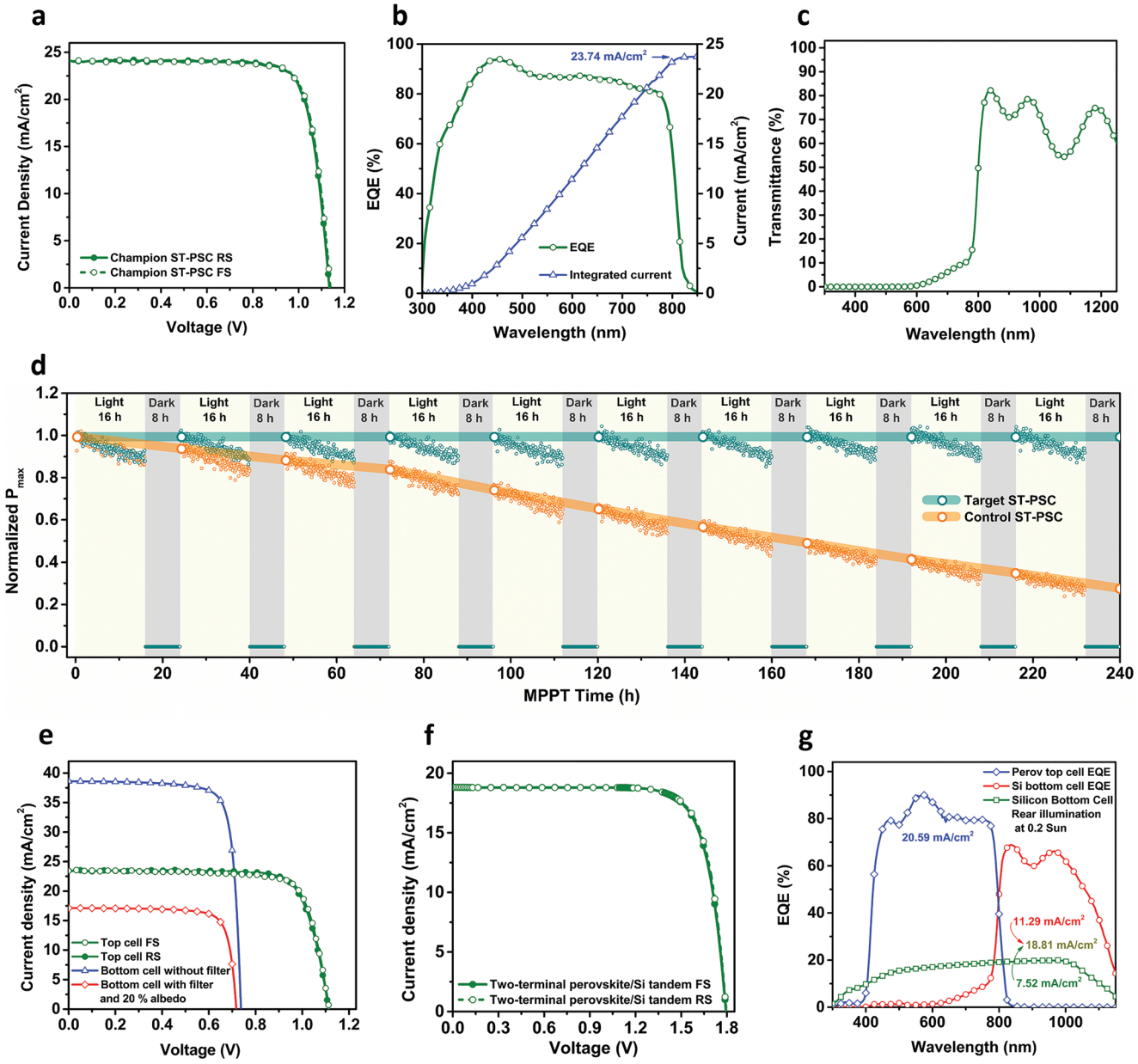

Figure 6. Characteristics of champion ST-PSC showing a) *J–V* curves, b) external quantum efficiency (EQE), c) transmittance, and d) MPPT results. e) *J–V* curves of top perovskite cell, bottom silicon cell (unfiltered and filtered at 20% albedo) in a four-terminal bifacial perovskite/silicon tandem solar cell configuration. f) *J–V* curves and g) EQE results of two-terminal bifacial perovskite/silicon tandem solar cell at 20% albedo.

certified PCE for a semi-transparent perovskite solar cell. The certified *I-V* measurements were conducted at PV device test laboratory in Korea Institute of Energy Research (KIER) which is an ISO/IEC17025 certified test center and accredited by Korea Laboratory Accreditation Scheme, which signed the International Laboratory Accreditation Cooperation-Mutual Recognition Arrangement.[52] Figure 6c shows the transmittance of our ST-PSC in the infra-red region of the spectrum (≈60%). Figure S18, Supporting Information shows the bandgap of the perovskite absorber (~1.524 eV) used in this work. In addition to the shelf-stability assessments of control and target ST-PSCs shown in Figure 2i, we further investigated their operational stability. It may be noted that impressive operational stability results obtained by maximum power point tracking (MPPT) of conventional opaque PSCs in recent years have mostly been obtained in testing environments where ambient stresses such as air and moisture exposure were eliminated by testing the devices either in inert environment (i.e., nitrogen),[17,18,42,53] or fully encapsulating the devices.[54] However, we used unencapsulated ST-PSCs in ambient air (RH of approximately 25% at room temperature) due to which our devices would be under added stress during MPPT compared to the above-mentioned reports. We followed the ISOS-LC-1 protocol (i.e., light-dark cycling under ambient conditions) for operational-stability assessments of PSCs.[55]

Table 3. *J–V* parameters of champion ST-PSC, silicon bottom cell, four and two-terminal bifacial perovskite/silicon tandem solar cells.

Device	Description	J_{SC} (mA cm^{-2})	V_{OC} (V)	FF	PCE (%)	Bifacial equivalent efficiency at 20% albedo (%)
Perovskite top cell (Champion ST-PSC, single junction)	Reverse *J–V* scan	24.07	1.138	0.804	22.04	-
	Forward *J–V* scan	24.13	1.134	0.804	21.99	-
	Reverse-forward scans averaged values	24.10	1.136	0.804	22.02	
	Certified values	23.74	1.139	0.801	**21.68**	-
Silicon bottom cell (Single junction)	Unfiltered front illumination	38.61	0.74	0.81	22.99	-
	Filtered front illumination and 20% albedo	17.12	0.72	0.80	-	9.82
4T bifacial tandem Cell	Front 1 Sun and 20% rear albedo	-	-	-	-	**31.50**
2T bifacial tandem cell (At front 1 Sun and 20% rear albedo)	Reverse J-V scan	18.81	1.79	0.78	-	26.34
	Forward J-V scan	18.81	1.79	0.78	-	26.34
	Certified values	18.81	1.79	0.78	-	**26.34**

Specifically, the cycle of illuminated MPPT for 16 h followed by dark operation for 8 h was repeated for 240 h as shown in Figure 6d. The control ST-PSC showed a continuous drop in P_{max} indicating poor stability whereas our target ST-PSC showed no long-term degradation for 240 h even under relatively harsh testing conditions. In case of target ST-PSC, although the P_{max} dropped to between 88–90% of its initial value for each light cycle of 16 h, it recovered back to 100% of its initial value after an 8 h dark cycle, showing a self-healing behavior. Such self-healing behavior of PSCs in the dark has been reported by several groups,[56–60] and it has been suggested that this self-healing behavior can practically enable the commercial operation of PSCs since it gives an opportunity for dark self-recovery every night after 10 to 12% photoinduced degradation during the day time operation.[58] A similar trend of maximum power (P_{max}) dropping to 88 – 90% of its original value for each light cycle and recovering back to 100% after a dark cycle was observed for the corresponding opaque PSCs with 23.95% PCE (23.47% certified) (Figures S19 and S20, and Table S1, Supporting Information) as well which suggests that the origin of this recoverable P_{max} drop is not the HTL/MoO_3 interface but rather the commonly reported photoinduced phenomena in the perovskite absorber itself which is beyond the scope of this study.

Finally, we applied our strategy of HTL surface modification with Li_xO_y to four- and two-terminal tandem configurations. For a four-terminal (4T) bifacial perovskite/Si tandem solar cell we used a certified 21.68% efficient champion ST-PSC as the top cell with a bifacial silicon heterojunction (HJT) bottom solar cell provided by Jusung Engineering Ltd. This 4T bifacial tandem solar cell enabled a 31.5% bifacial equivalent efficiency at 20% albedo (Figure 6e and Table 3). (Presently, an established standard for bifacial measurement of tandem solar cells lacks. The average global albedo is about 30%, however, we opted for a conservative use of albedo, i.e., 20% for our measurement.) In this measurement, the current density of the bottom cell was corrected to eliminate overestimation due to the back-reflection from the sample stage as shown in Figure S21, Supporting Information. Details regarding the measurement of 4T bifacial tandem solar cell are given in supplementary information and the detailed photovoltaic parameters are tabulated in Table S7, Supporting Information. We also fabricated a 1.1081 cm^2 two-terminal (2T) perovskite/silicon tandem solar cell and carried out *J–V* measurements under bifacial illumination with various albedos including 0, 20, 30, 40, and 100% as shown in Figure S22 and Table S8, Supporting Information which shows current saturation at 40% albedo. We also sent our tandem device for an official bifacial *J-V* measurement to PV device test laboratory at KIER where our 2T tandem device showed a bifacial equivalent efficiency of 26.34% at 20% albedo. 2T bifacial tandem solar cell *J-V* and EQE results are presented in Figure 6f and 6g, respectively, and the official test report is given in Figure S23, Supporting Information. The measurement scheme of bifacial 2T tandem measurement is illustrated in Figure S24, Supporting Information and the details regarding the measurement are provided in the supplementary information. The fabricated 2T tandem device showed a >99% shelf-stability for 400 h of dark storage under RH ~10% as shown in Figure S25, Supporting Information.

3. Conclusion

In summary, we identified HTL/MoO_3 interface in ST-PSCs to be responsible for their low performance and fast degradation compared to opaque devices. Our experimental evidence reveals that Li ion diffusion from the LiTFSI dopant used in Spiro-MeOTAD HTL to the MoO_3 buffer layer causes a reduction in the WF of MoO_3 consequently increasing the hole-injection barrier at HTL/MoO_3 interface which is detrimental to the efficiency and stability of ST-PSCs. We modified the HTL surface by forming stable Li_xO_y (Li_2O and/or Li_2O_2) and studied their role in mitigating Li^+ diffusion across HTL/MoO_3 interface. Our DFT and TOF-SIMS analyses present strong theoretical and experimental evidence for effective mitigation of Li^+ diffusion into MoO_3 by formation of Li_xO_y at the HTL surface. This conclusion is further supported by the significantly improved performance and stability evident by high fill factor values (80.1%), a record certified PCE of 21.68%, a shelf stability of > 99% for 400 h and an operational stability of > 99% for 240 h according to the ISOS-LC-1 protocol (continuous MPPT for 16 h followed by dark storage of

8 h). Considering that LiTFSI is widely used for state-of-the-art high-efficiency PSCs, this work reports a new Li-induced internal degradation mechanism unique to the ST-PSCs employing HTL/MoO_3/TCO structure and its practical solution. Finally, excellent bifacial equivalent efficiencies of 31.5% and 26.34% for four- and two-terminal bifacial tandem solar cells (active area >1.10 cm^2), respectively, at 20% albedo were achieved. This study opens a new perspective that organic semiconductors/oxides interfaces can be tuned to perform on par with the organic semiconductors/metallic interfaces in terms of interface charge transport, which has significant implications in the realm of optoelectronic devices.

4. Experimental Section

Materials: SnO_2 colloidal precursor (tin(IV) oxide, 15% in H_2O colloidal dispersion) was purchased from Alfa Aesar. 2-propanol (IPA), Chlorobenzene, Acetonitrile, bis(trifluoromethane) sulfonamide lithium salt (Li-TFSI), 4-tert-Butylpyridine, dimethyl sulfoxide (DMSO), lead iodide (PbI_2) and methyl ammonium chloride (MACl) were purchased from Sigma Aldrich. Formamidinium iodide (FAI), methylammonium iodide (MAI), n-Octylammonium iodide (OAI) were purchased from Greatcell Solar. Spiro-MeOTAD was purchased from Lumtec. All the chemicals were used as received without further purification.

Device Fabrication: *Fabrication of Opaque Perovskite Solar Cells*: Opaque PSCs were fabricated according to the procedures described by Jiang et. al.[42] Briefly, etched ITO glass substrates were sequentially cleaned with deionized water, acetone, and ethyl alcohol for 15 min each in a sonication bath. After drying the substrates, they were treated with plasma ozone for 10 mins to remove any organic residue from the surface and make it hydrophilic for improving the wettability. A thin film of SnO_2 nanoparticle (2.67 wt.%, diluted by deionized water) was spin-coated at 4,000 rpm for 30 s, and annealed at 150 °C for 30 min. After cooling the substrates to room temperature, 1.5 M solution of PbI_2 dissolved in DMF : DMSO (9 : 1 by vol) was spin-coated onto the SnO_2 layer at 1,500 rpm for 30 s followed by annealing at 70°C for 1 min. After cooling down the PbI_2 coated substrates, a solution of FAI : MAI : MACl (90 mg : 6.39 mg : 9 mg in 1 mL IPA) was spin-coated at 2,000 rpm for 30 s, the substrates were then heat treated at 150°C for 15 min. The perovskite absorber has a composition of $FA_{0.92}MA_{0.08}PbI_3$ and a bandgap of ≈1.53 eV. Followed by cooling the absorber, a 0.015 M OAI solution in IPA was dynamically spin-coated for interface passivation.[61] Then a hole-transport layer (HTL) consisting of Spiro-MeOTAD 72.3 mg, 35 µL Li-TFSI stock solution (260 mg Li-TFSI in 1 mL acetonitrile), 30 µL 4-tert-Butylpyridine and 1 mL chlorobenzene was spin-coated at 3,000 rpm for 30 s. All the solution-making processes except for SnO_2 solution were carried out in a nitrogen-filled glovebox, whereas SnO_2 solution was made in ambient conditions. All the spin-coating and annealing processes were carried out in a fume hood with controlled temperature (26 °C) and relative humidity of 20%–25%. It has been observed that spin-coating PbI_2 layer at temperatures lower than 25 °C or spin-coating the organic salts solution onto the PbI_2 layer at humidity lower than 10% results in V_{oc} and FF loss. Finally, using a shadow mask of contact area 0.143 cm^2 an 80 nm thick gold counter electrode was deposited by thermal evaporation under a high vacuum condition of $< 5 \times 10^{-6}$ Torr.

Fabrication of Semi-Transparent Perovskite Solar Cells (ST-PSCs): All the layers of ST-PSCs were fabricated exactly as described for opaque PSCs until HTL. After HTL deposition the devices were oxidized in a desiccator containing air with relative humidity below 10% for various time periods (3 h to 4 days). After that MoO_3 was thermally evaporated under a vacuum of 2×10^{-5} Torr. The optimum thickness of MoO_3 was experimentally determined to be 12 nm as shown in Figure S26a,b, Supporting Information as well as in Table S9, Supporting Information. The optimum thickness of 12 nm was analyzed by transmission electron microscope (TEM) image of a full device (Figure S26c, Supporting Information) and it corresponded to a QCM measured film thickness of 20 nm. The devices were then masked using a shadow mask and loaded into a sputtering chamber where 140 nm thick indium-doped zinc oxide (IZO) electrode was sputter deposited at a power of 50 W for 35 mins at a working pressure of 1 mTorr under an argon flow of 4 sccm. The optimum thickness of 140 nm for IZO was experimentally determined by fabricating and testing ST-PSCs with varying thicknesses of IZO (100, 120, 140, 170 and 200 nm) as shown in Figure S27a, Supporting Information. The photovoltaic parameters including V_{oc}, FF, J_{sc} and PCE shown in Figure S27c–f, Supporting Information as well as tabulated in Table S10, Supporting Information show that below 140 nm there are FF losses due to increased series resistance whereas above 140 nm there are J_{sc} losses without further improvements of FF, therefore 140 nm was used as optimum thickness of IZO which was also verified by TEM analysis. Finally, gold was selectively deposited via thermal evaporation for contacts. 110 nm of MgF_2 was thermally evaporated on the glass side of the champion ST-PSC as an anti-reflection coating.

Fabrication of Silicon Bottom Cells for 4T Tandem Solar Cells: Bifacial silicon bottom cells for four-terminal tandem solar cells were provided by Jusung Engineering Ltd.

Fabrication of Silicon Bottom Cells for 2T Tandem Solar Cells: Silicon heterojunction (SHJ) solar cells with front emitters were used as the bottom cells. Single side polished Float zone (FZ) wafers with thickness of 250 µm and resistivity of 7∼10 Ω.cm were used as substrates. The wafers were first cleaned with an ozone cleaning process followed by 1% diluted hydrofluoric acid dip. Afterwards, the wafers were transported into a plasma enhanced chemical vapor deposition (PECVD) tool for intrinsic and doped hydrogenated amorphous silicon (a-Si:H) fabrication. The rear intrinsic/n-type a-Si:H stack, front intrinsic a-Si:H and p-type a-Si:H were deposited in three chambers with thickness of 4 nm/4 nm, 6 nm, and 13 nm, respectively, where the n-side was on the textured side and p-side was on the polished side of the wafers. Then 70 nm and 20 nm ITO layers were sputtered on the n-side and p-side, respectively.

Fabrication of Two-Terminal Bifacial Silicon/Perovskite Tandem Solar Cells: The silicon bottom cells were cut into 25 cm x 25 cm size for spin-coating perovskite top cell layers onto it. The cut silicon bottom cells were cleaned and all the layers until HTL were deposited in the same manner as described in "*Fabrication of opaque Perovskite Solar Cell*" section. Afterward, the HTL was subjected to oxidation in desiccator for 4 days followed by thermal evaporation of a 12 nm thick MoO_3 buffer layer under a vacuum of 2×10^{-5} Torr. Next, an IZO transparent electrode was deposited via a shadow mask in the same manner as described in fabrication of ST-PSCs. Finally, a bilayer metallic grid consisting of a 300 nm thick Ni and a 1.6 µm thick Al was deposited using a multi-pocket e-beam evaporator under a vacuum of 2×10^{-6} Torr on both sides (front and rear) of the bifacial tandem device in two separate runs. The device has an illuminated area of 1.1081 cm^2. 110 nm of MgF_2 was thermally evaporated on both front and rear sides of the two-terminal tandem devices as anti-reflection coating.

Characterizations: *J–V analysis of Devices*: Single junction *J–V* measurements were performed at a simulated AM1.5 using a Newport Class AAA solar simulator and a Keithley 2410 source meter using Peccell software. The light intensity was calibrated to 100 mW cm^{-2} using a Si-reference cell certified by KIER. The illumination area was defined by a shadow mask with an aperture size of 0.071822 cm^2. The unencapsulated devices were measured in both the reverse scan (1.2 V to 0 V, step 0.02 V) and the forward scan (0 V to 1.2 V, step 0.02 V) at a search delay of 10 ms under ambient conditions (25% RH at 25°C). The samples were soaked under 1 Sun for 1 to 3 mins. During the *J–V* measurements samples were prevented from heating up by air cooling.

The bifacial equivalent efficiency (or gain efficiency) of bifacial four-terminal perovskite/Si tandem solar cell was calculated by adding (i) the separately measured certified PCE of ST-PSC (top cell) and (ii) the perovskite top cell-filtered bifacial equivalent efficiency of bottom cell at 20% albedo. Detailed procedure of this measurement is given in "*Measurement of bifacial 4T perovskite/Si tandem device*" section of the supporting information.

The *J–V* measurements of bifacial two-terminal perovskite/Si tandem solar cell were performed using SAN-EI, XHS-220S1 (Class-AAA)

simulator equipped with a specially designed bifacial measurement jig as illustrated in Figure S24, Supporting Information. The device was kept at 25.0 °C using air cooling. Detailed procedure of this measurement is given in "*Measurement of bifacial 2T perovskite/Si tandem device*" section of the supporting information.

EQE Measurements: The EQE of ST-PSCs was measured using a McScience K3100 Spectra IPCE Measurement System. The chopper frequency was kept at 4 Hz during measurement.

The EQE of bifacial silicon/perovskite 2T tandem solar cell was measured using S-9240 / HINODE mini5 spectral response measuring system by Soma. During top cell EQE measurement, the device was illuminated from the front using an 850 nm cut-on filter to eliminate the bottom cell EQE signal. Furthermore, the bottom cell was biased at its V_{oc} (0.65 V) during top cell EQE measurement. For bottom silicon cell EQE measurement a 450 nm cut-off filter was used and a bias equal to the V_{oc} of the top cell (1.1 V) was applied during the measurement. Finally, the effect of rear illumination (20% albedo) on the EQE signal of the tandem device was separately measured by using another bottom cell fabricated in the same batch as that used in the tandem. Its EQE at 1 Sun was measured and then it was converted into 0.2 Sun EQE (equivalent to 20% albedo).

MPPT Measurements: Maximum power point tracking (MPPT) measurements were made using a home-made setup consisting of an LED light source, Keithley 2400 source meter along with National Instruments interface. An unencapsulated device was measured at RH <25%, ~25°C in a cyclic manner for 16 h under illumination and 8 h recovered in dark (simulating day and night operation of a solar cell) according to the ISOS-LC-1 protocol.[55]

Other Characterizations: UV-Vis spectrometry measurements on HTL were made using UV-Vis Spectrophotometer UV-2600 by SHIMADZU. Bare HTL XPS measurements were made on XPS (Nexsa) by Thermoscientific. In-situ HTL/MoO_3 interface was analyzed by a hemispherical electron analyzer (SES-100, VG-Scienta), a He-I discharge lamp ($\hbar\omega = 21.2$ eV) for UPS, and a non-monochromatized Al Kα ($\hbar\omega = 1486.7$ eV) source for XPS. Time of flight secondary ion mass spectroscopy (tof-SIMS) measurements of HTL were made on ION-TOF (Munster, Germany) Model TOF.SIMS 5.

Supporting Information

Supporting Information is available from the Wiley Online Library or from the author.

Acknowledgements

This work was financially supported by the Korea Institute of Energy Research (KIER) grant (C3-2401, 2402, and 2403) and Korea Institute of Energy Technology Evaluation and Planning (KETEP) grand funded by the Korean government (MOTIE) (No. 20213030010400). The authors acknowledge Yun Jung Jang from the Korea Institute of Science and Technology (KIST) for helping perform the TOF-SIMS experiments. The authors also thank Suzanne Adam, PhD, from Edanz for editing a draft of this manuscript.

Conflict of Interest

The authors declare no conflict of interest.

Data Availability Statement

The data that support the findings of this study are available on request from the corresponding author. The data are not publicly available due to privacy or ethical restrictions.

Keywords

bifacial tandem solar cells, charge transport, lithium ions diffusion, lithium oxides, semi-transparent perovskite solar cells, stability

Received: July 5, 2023
Revised: October 13, 2023
Published online: October 30, 2023

[1] A. Kojima, K. Teshima, Y. Shirai, T. Miyasaka, *J. Am. Chem. Soc.* **2009**, *131*, 6050.
[2] *NREL Best Research-Cell Efficiencies Chart (Rev. 04-05-2023)*, **n.d**.
[3] "First building-integrated deployment shows perovskite solar's growing maturity | News | Chemistry World," can be found under, https://www.chemistryworld.com/news/first-building-integrated-deployment-shows-perovskite-solars-growing-maturity/3009953.article, **n.d**.
[4] B. Chen, S.-W. Baek, Y. Hou, E. Aydin, M. De Bastiani, B. Scheffel, A. Proppe, Z. Huang, M. Wei, Y.-K. Wang, E.-H. Jung, T. G. Allen, E. Van Kerschaver, F. P García De Arquer, M. I. Saidaminov, S. Hoogland, S. De Wolf, E. H. Sargent, *Nat. Commun.* **2020**, *11*, 1257.
[5] J. Peng, T. Duong, X. Zhou, H. Shen, Y. Wu, H. K. Mulmudi, Y. Wan, D. Zhong, J. Li, T. Tsuzuki, K. J. Weber, K. R. Catchpole, T. P. White, *Adv. Energy Mater.* **2017**, *7*, 1601768.
[6] K. Yang, F. Li, J. Zhang, C. P. Veeramalai, T. Guo, *Nanotechnology* **2016**, *27*, 095202.
[7] Z. Wang, X. Zhu, S. Zuo, M. Chen, C. Zhang, C. Wang, X. Ren, Z. Yang, Z. Liu, X. Xu, Q. Chang, S. Yang, F. Meng, Z. Liu, N. Yuan, J. Ding, S. (Frank) Liu, D. Yang, *Adv. Funct. Mater.* **2020**, *30*, 1908298.
[8] C. O. Ramírez Quiroz, Y. Shen, M. Salvador, K. Forberich, N. Schrenker, G. D. Spyropoulos, T. Heumüller, B. Wilkinson, T. Kirchartz, E. Spiecker, P. J. Verlinden, X. Zhang, M. A. Green, A. Ho-Baillie, C. J. Brabec, *J. Mater. Chem. A* **2018**, *6*, 3583.
[9] D. Yang, X. Zhang, Y. Hou, K. Wang, T. Ye, J. Yoon, C. Wu, M. Sanghadasa, S. F. Liu, S. Priya, *Nano Energy* **2021**, *84*, 105934.
[10] K. Aitola, K. Domanski, J.-P. Correa-Baena, K. Sveinbjörnsson, M. Saliba, A. Abate, M. Grätzel, E. Kauppinen, E. M. J. Johansson, W. Tress, A. Hagfeldt, G. Boschloo, W. Tress, A. Hagfeldt, G. Boschloo, *Adv. Mater.* **2017**, *29*, 1606398.
[11] Z. Li, S. A. Kulkarni, P. P. Boix, E. Shi, A. Cao, K. Fu, S. K. Batabyal, J. Zhang, Q. Xiong, L. H. Wong, N. Mathews, S. G. Mhaisalkar, *ACS Nano* **2014**, *8*, 6797.
[12] Y. (M.). Yang, Q. Chen, Y.-T. Hsieh, T.-B. Song, N. De Marco, H. Zhou, Y. Yang, *ACS Nano* **2015**, *9*, 7714.
[13] C. Roldán-Carmona, O. Malinkiewicz, R. Betancur, G. Longo, C. Momblona, F. Jaramillo, L. Camacho, H. J. Bolink, *Energy Environ. Sci.* **2014**, *7*, 2968.
[14] H. Shen, T. Duong, J. Peng, D. Jacobs, N. Wu, J. Gong, Y. Wu, S. K. Karuturi, X. Fu, K. Weber, X. Xiao, T. P. White, K. Catchpole, *Energy Environ. Sci.* **2018**, *11*, 394.
[15] C. Zhang, M. Chen, F. Fu, H. Zhu, T. Feurer, W. Tian, C. Zhu, K. Zhou, S. Jin, S. M. Zakeeruddin, A. N. Tiwari, N. P. Padture, M. Grätzel, Y. Shi, *Energy Environ. Sci.* **2022**, *15*, 1536.
[16] J. J. Yoo, G. Seo, M. R. Chua, T. G. Park, Y. Lu, F. Rotermund, Y.-K. Kim, C. S. Moon, N. J. Jeon, J.-P. Correa-Baena, V. Bulovic, S. S. Shin, M. G. Bawendi, J. Seo, *Nature* **2021**, *590*, 587.
[17] H. Min, D. Y. Lee, J. Kim, G. Kim, K. S. Lee, J. Kim, M. J. Paik, Y. K. Kim, K. S. Kim, M. G. Kim, T. J. Shin, S. Il Seok, *Nature* **2021**, *598*, 444.
[18] J. Jeong, M. Kim, J. Seo, H. Lu, P. Ahlawat, A. Mishra, Y. Yang, M. A. Hope, F. T. Eickemeyer, M. Kim, Y. J. Yoon, I. W. Choi, B. P. Darwich, S. J. Choi, Y. Jo, J. H. Lee, B. Walker, S. M. Zakeeruddin, L. Emsley, U. Rothlisberger, A. Hagfeldt, D. S. Kim, M. Grätzel, J. Y. Kim, *Nature* **2021**, *592*, 381.
[19] J. Werner, G. Dubuis, A. Walter, P. Löper, S.-J. Moon, S. Nicolay, M. Morales-Masis, S. De Wolf, B. Niesen, C. Ballif, *Sol. Energy Mater. Sol. Cells* **2015**, *141*, 407.

[20] P. Löper, S.-J. Moon, S. Martín De Nicolas, B. Niesen, M. Ledinsky, S. Nicolay, J. Bailat, J.-H. Yum, S. De Wolf, C. Ballif, *Phys. Chem. Chem. Phys.* **2015**, *17*, 1619.
[21] J. A. Christians, P. A. Miranda Herrera, P. V. Kamat, *J. Am. Chem. Soc.* **2015**, *137*, 1530.
[22] J. Yang, B. D. Siempelkamp, D. Liu, T. L. Kelly, *ACS Nano* **2015**, *9*, 1955.
[23] G. E. Eperon, S. D. Stranks, C. Menelaou, M. B. Johnston, L. M. Herz, H. J. Snaith, *Energy Environ. Sci.* **2014**, *7*, 982.
[24] W. Chen, Y. Wu, Y. Yue, J. Liu, W. Zhang, X. Yang, H. Chen, E. Bi, I. Ashraful, M. Grätzel, L. Han, **2015**, *Science 350*, 944.
[25] J. Lim, M. Kim, H. H. Park, H. Jung, S. Lim, X. Hao, E. Choi, S. Park, M. Lee, Z. Liu, M. A. Green, J. Seo, J. Park, J. S. Yun, *Sol. Energy Mater. Sol. Cells* **2021**, *219*, 110776.
[26] H. J. Snaith, M. Grätzel, *Appl. Phys. Lett.* **2006**, *89*, 262114.
[27] A. Abate, T. Leijtens, S. Pathak, J. Teuscher, R. Avolio, M. E. Errico, J. Kirkpatrik, J. M. Ball, P. Docampo, I. Mcpherson, H. J. Snaith, *Phys. Chem. Chem. Phys.* **2013**, *15*, 2572.
[28] S. Moghadamzadeh, I. M. Hossain, M. Jakoby, B. Abdollahi Nejand, D. Rueda-Delgado, J. A. Schwenzer, S. Gharibzadeh, T. Abzieher, M. R. Khan, A. A. Haghighirad, I. A. Howard, B. S. Richards, U. Lemmer, U. W. Paetzold, *J. Mater. Chem. A* **2020**, *8*, 670.
[29] Y. Wang, H. Qu, C. Zhang, Q. Chen, *Sci. Rep.* **2019**, *9*, 459.
[30] A. Agresti, S. Pescetelli, L. Cinà, D. Konios, G. Kakavelakis, E. Kymakis, A. Di Carlo, *Adv. Funct. Mater.* **2016**, *26*, 2686.
[31] G. Liu, X. Xi, R. Chen, L. Chen, G. Chen, *J. Renewable Sustainable Energy* **2018**, *10*, https://doi.org/10.1063/1.5031167.
[32] Z. Li, C. Xiao, Y. Yang, S. P. Harvey, D. H. Kim, J. A. Christians, M. Yang, P. Schulz, S. U. Nanayakkara, C.-S. Jiang, J. M. Luther, J. J. Berry, M. C. Beard, M. M. Al-Jassim, K. Zhu, *Energy Environ. Sci.* **2017**, *10*, 1234.
[33] C. Ding, R. Huang, C. Ahläng, J. Lin, L. Zhang, D. Zhang, Q. Luo, F. Li, R. Österbacka, C.-Q. Ma, *J. Mater. Chem. A* **2021**, *9*, 7575.
[34] Z. Hawash, L. K. Ono, S. R. Raga, M. V. Lee, Y. Qi, *Chem. Mater.* **2015**, *27*, 562.
[35] F. Bonino, L. Bicelli, B. Rivolta, M. Lazzari, F. Festorazzi, *Solid State Ionics* **1985**, *17*, 21.
[36] J. Besenhard, J. Heydecke, E. Wudy, H. Fritz, W. Foag, *Solid State Ionics* **1983**, *8*, 61.
[37] M. S Whittingham, *J. Electrochem. Soc.* **1976**, *123*, 315.
[38] S.-H. Lee, Y.-H. Kim, R. Deshpande, P. A. Parilla, E. Whitney, D. T. Gillaspie, K. M. Jones, A. H Mahan, S. Zhang, A. C. Dillon, *Adv. Mater.* **2008**, *20*, 3627.
[39] M. F. Hassan, Z. P. Guo, Z. Chen, H. K. Liu, *J. Power Sources* **2010**, *195*, 2372.
[40] R. Schölin, M. H. Karlsson, S. K. Eriksson, H. Siegbahn, E. M. J. Johansson, H. Rensmo, *J. Phys. Chem. C* **2012**, *116*, 26300.
[41] Q. Jiang, Z. Chu, P. Wang, X. Yang, H. Liu, Y. Wang, Z. Yin, *Adv. Mater.* **2017**, *29*, 1703852.
[42] Q. Jiang, Y. Zhao, X. Zhang, X. Yang, Y. Chen, Z. Chu, Q. Ye, X. Li, Z. Yin, J. You, *Nat. Photonics* **2019**, *13*, 460.
[43] R. L. Forward, K. Y. Chen, D. M. Weekes, D. J. Dvorak, Y. Cao, C. P. Berlinguette, *ACS Energy Lett.* **2019**, *4*, 2547.
[44] T. J. Quill, G. Lecroy, A. Melianas, D. Rawlings, Q. Thiburce, R. Sheelamanthula, C. Cheng, Y. Tuchman, S. T. Keene, I. Mcculloch, R. A. Segalman, M. L. Chabinyc, A. Salleo, *Adv. Funct. Mater.* **2021**, *31*, 2104301.
[45] S. Thinius, M. M. Islam, P. Heitjans, T. Bredow, *J. Phys. Chem. C* **2014**, *118*, 2273.
[46] M. T. Greiner, M. G. Helander, W.-M. Tang, Z.-B. Wang, J. Qiu, Z.-H. Lu, *Nat. Mater.* **2012**, *11*, 76.
[47] J. Meyer, S. Hamwi, M. Kröger, W. Kowalsky, T. Riedl, A. Kahn, *Adv. Mater.* **2012**, *24*, 5408.
[48] M. Kröger, S. Hamwi, J. Meyer, T. Riedl, W. Kowalsky, A. Kahn, *Appl. Phys. Lett.* **2009**, *95*, 4.
[49] H. Zhang, T. Stubhan, N. Li, M. Turbiez, G. J. Matt, T. Ameri, C. J. Brabec, *J. Mater. Chem. A* **2014**, *2*, 18917.
[50] Y. Hou, X. Du, S. Scheiner, D. P. Mcmeekin, Z. Wang, N. Li, M. S. Killian, H. Chen, M. Richter, I. Levchuk, N. Schrenker, E. Spiecker, T. Stubhan, N. A. Luechinger, A. Hirsch, P. Schmuki, H.-P. Steinrück, R. H. Fink, M. Halik, H. J. Snaith, C. J. Brabec, *Science* **2017**, *358*, 1192.
[51] Z. Hawash, L. K. Ono, Y. Qi, *Adv. Mater. Interfaces* **2016**, *3*, 1600117.
[52] "ILAC MRA and Signatories International Laboratory Accreditation Cooperation," can be found under https://ilac.org/ilac-mra-and-signatories/, **n.d**.
[53] S. You, F. T. Eickemeyer, J. Gao, J.-H. Yum, X. Zheng, D. Ren, M. Xia, R. Guo, Y. Rong, S. M. Zakeeruddin, K. Sivula, J. Tang, Z. Shen, X. Li, M. Grätzel, *Nat. Energy* **2023**, *8*, 515.
[54] M. Kim, J. Jeong, H. Lu, T. K. Lee, F. T. Eickemeyer, Y. Liu, I. W. Choi, S. J. Choi, Y. Jo, H.-B. Kim, S.-I. Mo, Y.-K. Kim, H. Lee, N. G. An, S. Cho, W. R. Tress, S. M. Zakeeruddin, A. Hagfeldt, J. Y. Kim, M. Grätzel, D. S. Kim, *Science* **2022**, *375*, 302.
[55] M. V. Khenkin, E. A. Katz, A. Abate, G. Bardizza, J. J. Berry, C. Brabec, F. Brunetti, V. Bulovic, Q. Burlingame, A. Di Carlo, R. Cheacharoen, Y.-B. Cheng, A. Colsmann, S. Cros, K. Domanski, M. Dusza, C. J. Fell, S. R. Forrest, Y. Galagan, D. Di Girolamo, M. Grätzel, A. Hagfeldt, E. Von Hauff, H. Hoppe, J. Kettle, H. Köbler, M. S. Leite, S. Liu, Y.-L. Loo, J. M. Luther, et al., *Nat. Energy* **2020**, *5*, 35.
[56] D. R. Ceratti, Y. Rakita, L. Cremonesi, R. Tenne, V. Kalchenko, M. Elbaum, D. Oron, M. A. C. Potenza, G. Hodes, D. Cahen, *Adv. Mater.* **2018**, *30*, 1706273.
[57] M. Bag, L. A. Renna, R. Y. Adhikari, S. Karak, F. Liu, P. M. Lahti, T. P. Russell, M. T. Tuominen, D. Venkataraman, *J. Am. Chem. Soc.* **2015**, *137*, 13130.
[58] K. Domanski, B. Roose, T. Matsui, M. Saliba, S.-H. Turren-Cruz, J.-P. Correa-Baena, C. R. Carmona, G. Richardson, J. M. Foster, F. De Angelis, J. M. Ball, A. Petrozza, N. Mine, M. K. Nazeeruddin, W. Tress, M. Grätzel, U. Steiner, A. Hagfeldt, A. Abate, W. Tress, M. Grätzel, U. Steiner, A. Hagfeldt, A. Abate, *Energy Environ. Sci.* **2017**, *10*, 604.
[59] W. Nie, J. C. Blancon, A. J. Neukirch, K. Appavoo, H. Tsai, M. Chhowalla, M. A. Alam, M. Y. Sfeir, C. Katan, J. Even, S. Tretiak, J. J. Crochet, G. Gupta, A. D. Mohite, *Nat. Commun.* **2016**, *7*, 11574.
[60] P. Yadav, D. Prochowicz, E. A. Alharbi, S. M. Zakeeruddin, M. Grätzel, *J. Mater. Chem. C* **2017**, *5*, 7799.
[61] H. Kim, S. U. Lee, D. Y. Lee, M. J. Paik, H. Na, J. Lee, S. Il Seok, *Adv. Energy Mater.* **2019**, *9*, 1902740.